PCCP

Surface Characterization and Methane activation on SnOx/Cu2O/Cu(111) Inverse Oxide/Metal Catalysts

Journal:	*Physical Chemistry Chemical Physics*
Manuscript ID	CP-ART-06-2021-002829.R1
Article Type:	Paper
Date Submitted by the Author:	20-Jul-2021
Complete List of Authors:	Kang, Jindong ; Stony Brook University, Chemistry Rui, Ning; Brookhaven National Laboratory, Department of Chemistry Huang, Erwei; Stony Brook University, Chemistry Tian, Yi ; Stony Brook University, Chemistry Mahapatra, Mausumi; Brookhaven National Laboratory, Chemistry Rosales, Rina; Stony Brook University, Chemistry Orozco, Ivan; Stony Brook University Shi, Rui; Stony Brook University, Chemistry Senanayake, Sanjaya; Brookhaven National Laboratory, Chemistry Department Liu, Ping; Brookhaven National Laboratory, Chemistry Rodriguez, Jose; Brookhaven National Laboratory, Chemistry Department

ARTICLE

Surface Characterization and Methane activation on $SnO_x/Cu_2O/Cu(111)$ Inverse Oxide/Metal Catalysts†

Received 00th June 20xx,
Accepted 00th June 20xx

DOI: 10.1039/x0xx00000x

Jindong Kang,[‡a] Ning Rui,[‡b] Erwei Huang,[‡a] Yi Tian,[a] Mausumi Mahapatra,[b] Rina Rosales,[a] Ivan Orozco,[a] Rui Shi,[a] Sanjaya D. Senanayake,[b] Ping Liu,[a,b] and José A. Rodriguez*[a,b]

To activate methane at low or medium temperatures is a difficult task and a pre-requisite for the conversion of this light alkane into high value chemicals. Herein, we report the preparation and characterizations of novel $SnO_x/Cu_2O/Cu(111)$ interfaces that enable low-temperature methane activation. Scanning tunneling microscopy identified small, well-dispersed SnO_x nanoclusters on the $Cu_2O/Cu(111)$ substrate with an average size of 8 Å, and such morphology was sustained up to 450 K in UHV annealing. Ambient pressure X-ray photoelectron spectroscopy showed that hydrocarbon species (CH_x groups), the product of methane activation, were formed on $SnO_x/Cu_2O/Cu(111)$ at a temperature as low as 300 K. An essential role of the SnO_x-Cu_2O interface was evinced by the SnO_x coverage dependence. Systems with a small amount of tin oxide, 0.1 – 0.2 ML coverage, produced the highest concentration of adsorbed CH_x groups. Calculations based on density functional theory showed a drastic reduction in the activation barrier for C-H bond cleavage when going from $Cu_2O/Cu(111)$ to $SnO_x/Cu_2O/Cu(111)$. On the supported SnO_x, the dissociation of methane was highly exothermic (ΔE ~ -35 kcal/mol) and the calculated barrier for activation (~ 20 kcal/mol) could be overcome at 300-500 K, target temperatures for the conversion of methane to high value chemicals.

Introduction

Methane (CH_4) is the major constituent of abundant low-cost natural gas. However, the efficient use of methane as a starting point in the synthesis of commodity chemicals is difficult due to the high stability of the molecule and this light alkane is frequently combusted with O_2 for heating and electrical power generation, producing CO_2, which is a main greenhouse gas.[1,2] In this regard, a significant amount of research has been aimed at taking full advantage of this abundant resource and its direct conversion to valuable chemicals. For instance, methane to methanol conversion including steam reforming, dry reforming of methane to methanol via syngas, and direct methane oxidation to methanol has received enormous attention since methanol is a broadly used feedstock in the chemical industry and enables easy transportation.[3–11]

The current industrial synthesis of methanol from methane is accomplished via a two-step process: steam reforming of methane to syngas followed by the high-pressure catalytic conversion of the syngas to methanol. However, this method is energy and cost ineffective[2,5,12]. Hence, the direct conversion of methane to methanol is considered as a dream reaction by skipping extra steps and consequently providing economic advantages. To convert methane to methanol or other chemicals, methane first should be activated, but this process generally requires high energies because the light alkane has low electron and proton affinities, low polarity, high ionization energy, and strong C-H bonds (439.3 kJ/mol). To reduce the energy cost, the surface of a catalyst must be used for methane activation at low or moderate temperatures, conditions that would prevent the overoxidation or complete oxidation to CO or CO_2, which are favoured processes above 600 K.[4,5,13–15]

In the enzyme methane monooxygenase, the transformation of CH_4 into CH_3OH at room temperature is carried out a by a group of three copper cations.[16,17] This fact has motivated many studies examining the performance of copper cations contained in oxide lattices or in zeolite frameworks.[17,18] A few of these systems yield methanol but only when water is used for extraction or it is added to the reaction feed ($CH_4/O_2/H_2O$).[17,18] Recently, $CeO_2/Cu_2O/Cu(111)$ catalysts showed room temperature methane activation and directly produced methanol with a reactant mixture of CH_4, O_2, and H_2O, achieving 77% selectivity at 450 K, but when water was removed from the reaction feed the selectivity towards methanol dropped below 5%.[19,20] This finding has motivated our interest to identify new oxide-on-oxide configurations that can enhance the reactivity of the $Cu_2O/Cu(111)$ substrate to activate methane and eventually could be used as efficient catalysts for a $2CH_4 + O_2 \rightarrow 2CH_3OH$ transformation.

[a] Department of Chemistry, SUNY at Stony Brook, Stony Brook, NY, 11794 USA.
[b] Chemistry Department, Brookhaven National Laboratory, Upton, NY, 11973 USA.

†Electronic Supplementary Information (ESI) available: XPS spectra of pristine Au(111), Sn/Au(111) 0.1 and 0.6 ML $SnO_2/Cu_2O/Cu(111)$ surfaces, Bader charge analysis, distribution of Sn^{4+} and Sn^{2+} for $Sn_xO_y/Cu_2O/Cu(111)$ models, oxygen vacancy formation. See DOI: 10.1039/x0xx00000x

‡ All these authors contributed in equal terms to this research.

In the past, SnO_x has shown high sensitivity to methane, and many commercial gas sensors include SnO_2[21,22]. Plus, Sn and SnO_x have been adopted as promoters of catalysts in a variety of processes such as dry reforming and steam reforming of methane[23,24], partial oxidation of methane[25], and catalytic methane combustion[26]. On the other hand, copper and its oxides have proven its excellent catalytic performance in various methanol related reactions: methanol oxidation[27], methanol steam reforming[28] and methanol synthesis[29,30]. Therefore, combining two catalytically promising oxide candidates and expecting synergistic effects within the SnO_x-Cu_2O interface, we investigated the growth of tin oxide nanostructures on the Cu_2O/Cu(111) substrate. In this work, single atom like SnO_x nanoclusters were stabilized on the Cu_2O films and scanning tunnelling microscopy (STM), ambient-pressure x-ray photoelectron spectroscopy (AP-XPS), and calculations based on density-functional theory (DFT) were combined to elucidate the morphology, growth mechanism, and active sites of SnO_x/Cu_2O/Cu(111) surfaces for methane activation. In fact, the SnO_x-Cu_2O interface plays an important role in methane activation at a temperature as low as 300 K.

Experimental

Scanning Tunneling Microscopy (STM)

All the STM experiments were conducted using an Omicron STM instrument housed in an ultra-high vacuum chamber with a background pressure of 5×10^{-10} Torr. A Cu(111) single crystal (Princeton Scientific Corp) was cleaned by cycles of Ar ion sputtering (2 kV, 15 min) and annealing (650 K, 20 min). The STM images were collected at room temperature by using a Pt–Ir tip. The Cu_2O overlayer was prepared by exposing the Cu(111) surface to 5 x 10^{-7} torr of O_2 at 550 K for 15 min. Tin was vapor-deposited at 450 K on the pre-existing Cu_2O/Cu(111) surface under an atmosphere of oxygen (5 x 10^{-7} torr). For thermal stability tests, as prepared SnO_x/Cu_2O/Cu(111) surfaces were annealed to 360, 450, and 550K, consecutively. The preparation methods for our SnO_x films on the Cu_2O/Cu(111) substrate were adapted from those of our previously reported study examining the growth of ZnO films with the aim of generating active catalysts for methanol synthesis from CO_2 hydrogenation.[31,32]

Before acquiring the STM images, to minimize possible effects of tip shape, the tip was made as sharp as possible. In the data analysis, we took an average of all the SnO_x particles which appeared in the images to determine size instead of using a single value.

Ambient pressure X-ray Photoelectron Spectroscopy (AP-XPS)

The AP-XPS experiments were conducted using an instrument available at the Chemistry Department of Brookhaven National Laboratory (BNL). A Cu(111) single crystal, cleaned by cycles of Ar ion sputtering and annealing (800 K, 10 min), was used as a substrate to grow the Cu_2O films. Nanoclusters of SnOx were deposited following the same methodology applied in the STM experiments described above. The prepared surfaces were exposed to 50 mTorr of CH4 at 300 - 500 K while performing the AP-XPS measurements. A photon energy of 1253.6 eV (Mg K-α source) was used to acquire the Sn 3d, O 1s, C 1s, Cu 2p, and Cu LMM spectra. The spectra were recorded using a PHOIBOS 150 EP MCD-9 analyzer.

A. Density Functional Theory (DFT) Calculations

A spin polarized density functional theory (DFT)[33,34] implemented in Vienna *ab initio* simulation package (VASP)[35] was used to perform all the calculations. A 400 eV kinetic energy cutoff and the projector augmented wave method (PAW)[36,37] together with GGA exchange-correlation functional plus the PBE functional[38] were employed. Monkhorst-Pack[39] meshes with 3×3×1 were used to sample the Brillouin zone for all the surface calculations while meshes with gamma point were employed for all gas-phase species. The nudged elastic band method (NEB)[40] for each elementary reaction intermediates were performed to derive the transition states. The criteria for total energies and forces on all atoms were set as 10^{-5} eV and 0.02 eV $Å^{-1}$ for convergence, respectively. Gaussian smearing with width 0.05 eV was used to improve the convergence. The Cu (3p, 3d, 4s), Sn (4d, 5s, 5p), C (2s, 2p), O (2s, 2p) and H (1s) electrons were treated as valence states, while the remaining electrons were kept frozen as core states.

The SnO_2/Cu_2O/Cu(111) catalyst was modelled with 3 layers of a 4×4 Cu(111) surface and one monolayer of Cu_mO (m ≈ 1.13, see details in Fig. S1 for Cu_mO model construction and justifications) with Sn_xO_{2x} (x =1,2,3,4 in this study) cluster deposited on top (See main text for side view structures) to address the observed small SnO_2 particles in STM. The Hubbard-like U term[41] was considered to address Cu 3d electrons for the Cu_xO surface (U_{eff} = 5.2)[42], in which the Coulomb U and exchange J parameters were combined into a single parameter U_{eff} = U - J. During DFT optimizations, bottom two layers were fixed while the rests were allowed to relax with adsorbates.

Overall, the adsorption energy of adsorbate on the SnO_2/Cu_2O/Cu(111) model surface was calculated as:

$$\Delta E\ ads = E(Adsorbate/Surface) - E(surface) - E(adsorbate) \qquad \text{Eq. (1)}$$

where E is the total energy obtained from DFT calculations incorporated with zero-point energy (ZPE) correction E_{ZPE}:

$$E_{ZPE} = \sum_i^{number\ of\ modes} \frac{1}{2} h\nu_i \qquad \text{Eq. (2)}$$

where ν_i is calculated vibrational frequency by harmonic normal mode approximation for each intermediate.

B. Ab Initio Thermodynamics Analysis

To explore the stabilities of SnO_x clusters depositing on top of Cu_2O/Cu(111) catalyst under the experimental environments, ab initio thermodynamics analysis was utilized.[43,44] The

following equilibrium reaction was considered to study the effects of temperature (T), pressures (P) of oxygen and tin.

$xSn + xO_2 + Cu_2O/Cu(111) \rightleftharpoons Sn_xO_{2x}/Cu_2O/Cu(111)$ Reaction (1)

The Gibbs free energy ΔG for reaction (1) could be written as equation (Eq.) (3):

$$\Delta G(T,P) = G^s_{Sn_xO_{2x}/Cu_2O/Cu(111)} - G^s_{Cu2O/Cu(111)} - x\mu^g_{Sn} - 2x\mu^g_O \quad \text{Eq. (3)}$$

The Gibbs free energies of $Sn_xO_y/Cu_2O/Cu(111)$ and $Cu_2O/Cu(111)$ are approximated as their ZPE-corrected DFT calculated total energies, $E_{Sn_xO_{2x}/Cu_2O/Cu(111)}$ and $E_{Cu_2O/Cu(111)}$ respectively. The chemical potential of Sn and O_2 depend on the environmental T and P. The reference states of Sn and O at 0K was set as ZPE-corrected DFT calculated total energies for metallic Sn bulk ($E_{Sn_{bulk}}$) and half O_2 ideal gas molecule ($\frac{1}{2}E_{O_2}$). Thus, the chemical potential of Sn and O_2 at environmental T and P could be interpreted by the following equations:

$$\mu_{Sn}(T,P) = E_{Sn_{bulk}} + \Delta\mu_{Sn}(T,P) \quad \text{Eq. (4)}$$

$$\mu_O(T,P) = \frac{1}{2}E_{O_2} + \Delta\mu_O(T,P) \quad \text{Eq. (5)}$$

Where

$$\Delta\mu_{Sn}(T,P) = \Delta\mu_{Sn}(T,P^0) + RT\ln(P_{Sn}/P^0_{Sn}) = [\Delta\mu_{Sn}(T,P^0) + RT\ln(P_{Sn}/P^0_{Sn})] = \{H(T,P^0,Sn) - H(0K,P^0,Sn) - T[S(T,P^0,Sn) - S(0K,P^0,Sn)] + RT\,ln(P_{Sn}/P^0_{Sn})\} \quad \text{Eq. (6)}$$

and

$$\Delta\mu_O(T,P) = \Delta\mu_O(T,P^0) + \frac{1}{2}RT\ln(P_{O_2}/P^0_{O_2}) = \frac{1}{2}[\Delta\mu_{O_2}(T,P^0) + RT\ln(P_{O_2}/P^0_{O_2})] = \frac{1}{2}\{H(T,P^0,O_2) - H(0K,P^0,O_2) - T[S(T,P^0,O_2) - S(0K,P^0,O_2)] + RT\ln(P_{O_2}/P^0_{O_2})\} \quad \text{Eq. (7)}$$

The enthalpies (H) and entropies (S) in the Eq. (6) and Eq. (7) were taken from thermodynamic tables at standard pressure (P^0=1 atm) in NIST database[45].

By incorporating Eq. (4), Eq. (5) and ZPE-corrected DFT-calculated total energies for $Sn_xO_y/Cu_2O/Cu(111)$ and $Cu_2O/Cu(111)$ into Eq. (3), we now have:

$$\Delta G(T,P) = \Delta E - x\Delta\mu_{Sn}(T,P) - y\Delta\mu_O(T,P) \quad \text{Eq. (8)}$$

Where

$$\Delta E = E_{Sn_xO_{2x}/Cu_2O/Cu(111)} - E_{Cu_2O/Cu(111)} - xE_{Sn} - xE_{O_2} \quad \text{Eq. (9)}$$

By using Eq. (8), we could compare the stability of different Sn_xO_y clusters when depositing on top of $Cu_2O/Cu(111)$ catalyst under the experimental environments, as reported in our previous study.[46]

Results and discussion

A. Growth of SnO_x on $Cu_2O/Cu(111)$: STM and XPS Studies

A well-ordered Cu_2O surface was prepared by exposing the Cu(111) surface to 5 x 10^{-7} torr O_2 at 550 K[47–49] and probed by STM, as shown in Fig 1a. We had the typical structure seen before for thin films of Cu_2O on the copper substrate.[47,49] In the copper oxide film of Fig 1a, there are lattice defects and

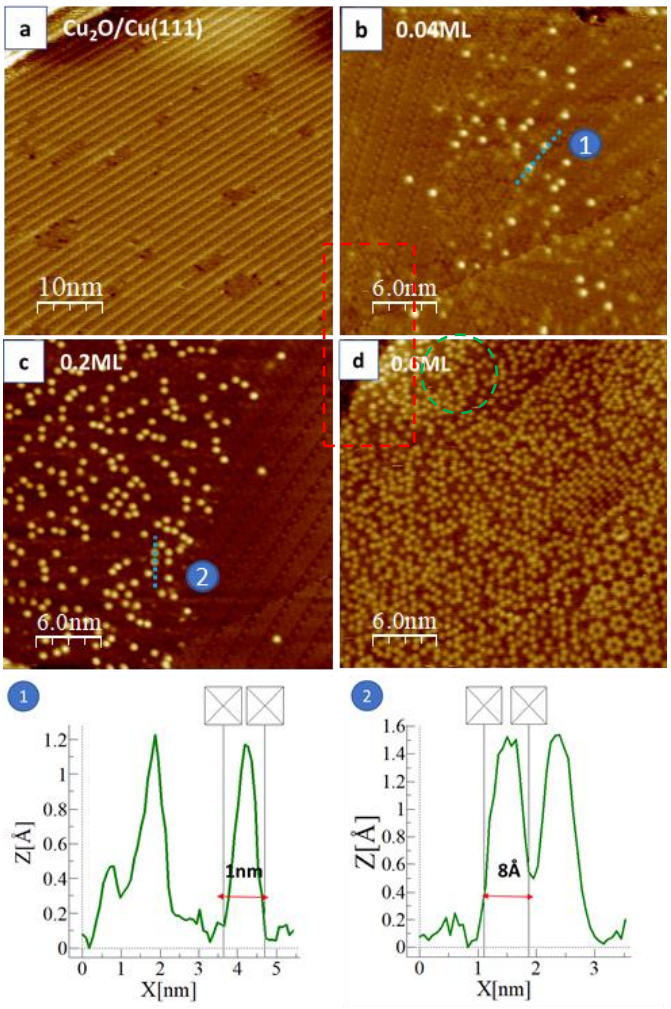

Fig. 1 Deposition of Sn on $Cu_2O/Cu(111)$ surface in 5 x 10^{-7} Torr of oxygen at 450 K (a) A clean $Cu_2O/Cu(111)$ surface, 50 x 50 nm^2. (b) 0.04 ML $SnO_x/Cu_2O/Cu(111)$, 30 x 30 nm^2 (c) 0.2 ML $SnO_x/Cu_2O/Cu(111)$, 30 x 30nm^2. The Cu_2O structure where SnO_x locates transformed. (d) 0.6 ML $SnO_x/Cu_2O/Cu(111)$, 30 x 30nm^2.The life profiles 1 and 2 show a representative size of SnOx clusters. Scanning conditions: (a) 0.1 nA, -1.2 V, (b) 0.1n A, 1.1 V, (c) 0.1n A, -1.4 V (d) 0.1n A, -1.4 V.

groups of oxygen vacancies. Fig 1b depicts a 0.04 ML (monolayer) coverage of tin deposition on the Cu_2O/Cu(111) surface under a background pressure of 5 x 10^{-7} torr of O_2 at 450 K. Higher coverages of SnO_x were prepared by increasing the amount of Sn deposition, and Fig 1c and 1d correspond to 0.2 and 0.6 ML. The bright dots in the figures represent SnO_x nanoclusters, and the size and height of the nanoclusters are in the range of 5 ~ 12 Å and 1 ~ 1.6 Å, respectively, according to the line profile measurements.

Interestingly, the SnO_x nanoclusters influenced the Cu_2O structure, leading to new morphologies where two different Cu_2O surface structures were observed on both 0.04 and 0.2 ML samples. In Fig 1b, the Cu_2O surrounded by SnO_x nanoclusters in the middle (marked by a green circle) shows a hexagonal ring structure, which is probably a reduced form of surface copper oxide,[47,49] and the area on the left (marked by a red retangle) shows no SnO_x and the intact Cu_2O structure. Additionally. the SnO_x nanocluster tends to reside on the hexagonal ring copper oxide surface preferentially, evidenced by Fig 1c where many nanoclusters are found on the left whereas very few exists on the well-ordered Cu_2O surface on the right. To further study the SnO_x growth mode, 0.6 ML coverage of the SnO_x/Cu_2O/Cu(111) surface was investigated, and the SnO_x clusters were observed to grow two-dimensionally on the Cu_2O surface instead of forming any three-dimensional islands, which indicates a strong interaction between SnO_x and the Cu_2O with a modification of the oxide substrate. Additionally, the underlying Cu_2O substrate influenced the structure of SnO_x, and at 0.6 ML, the hexagonal ring formation of SnO_x on the bottom right corner in Fig 1d was observed as the result of that. The Cu_2O/Cu(111) is known

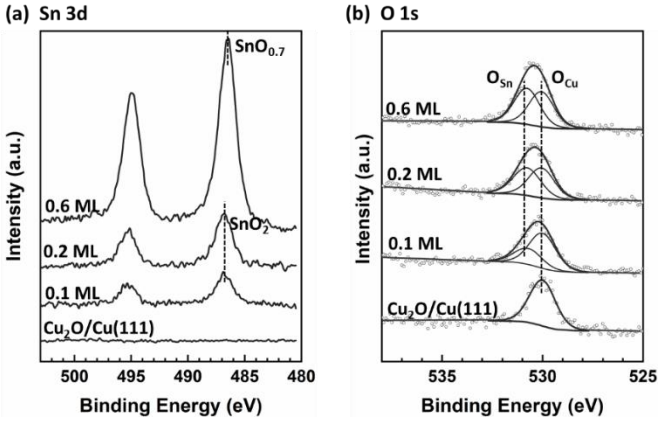

Fig. 2 (a) Sn 3d and (b) O 1s XPS spectra of pristine a Cu_2O/Cu(111) surface and SnO_x/Cu_2O/Cu(111) systems with different coverages. The SnO_x coverages in the samples were estimated to be 0.1, 0.2, and 0.6 ML.

for its hexagonal structure with a periodicity of ~ 6 Å and the O – O distance is 6.03 Å.[50] The measured distance across the SnOx clusters within the hexagon in Figure 1d is 12 Å and this show a good lattice match between the Cu_2O substrate and the hexagonal shape of SnO_x clusters.

XPS was used to probe the chemical states of the SnO_x/Cu_2O/Cu(111) surfaces. These SnO_x/Cu_2O/Cu(111) systems with different coverages were prepared following the same protocol as described above in the STM section. As shown in Fig 2(a), the binding energy of the Sn $3d_{5/2}$ peak is 486.8 eV for the 0.1 and 0.2 ML samples, consistent with the reported data for SnO_2 [51,52]. In contrast, the binding energy of the 0.6 ML sample is shifted by 0.3 eV to 486.5 eV, indicating that Sn is in a lower valence state. It has been reported that the binding energies of SnO_2 and SnO are very close, with only a 0.2 eV difference. To better identify the valence state of Sn, a deconvolution was carried out for the O 1s data, as shown in Fig 2(b). The oxygen signal can be deconvoluted into two peaks coming from O atoms interacting with Cu (O_{Cu}) at 530.0 eV and with Sn (O_{Sn}) at 530.8 eV. The Scofield relative sensitive factor (R.S.F.) was used to calculate O/Sn atomic ratio.[53] Interestingly, for the 0.1 and 0.2 ML systems, the O/Sn ratio was around 2, while it was only 0.7 for the 0.6 ML sample. This result confirms that the oxidation state of Sn is 4+ for the 0.1 and 0.2 ML samples, and around 1.4+ for the 0.6 ML sample. These results are consistent with the observations based on shifts for the Sn 3d binding energy as mentioned above.

An important point that needs to be mentioned here is that when Sn is deposited onto a Au(111) surface under oxygen ambient instead of Cu_2O/Cu(111), it is in the metallic or surface alloy state. The corresponding Sn 3d and O 1s XPS spectra for Sn/Au(111) are shown in Fig S2. An essential difference between Au(111) and Cu_2O/Cu(111) surface is that Au(111) is inert and no oxygen atom is present on the surface, while the Cu_2O/Cu(111) substrate is rich in O atoms. Therefore, we conclude that Sn has a strong interaction with O atoms of the Cu_2O/Cu(111) surface. Once Sn is deposited onto Cu_2O/Cu(111) surface, it will be auto-oxidized. This conclusion is also consistent with the STM images in Figure 1 (b) and (c), which shows that the Cu_2O is modified after the deposition of 0.04 and 0.2 ML of Sn. The images reflect that not only underneath but also the surrounding O atoms from Cu_2O will interact with Sn to form SnO_2. For the 0.6 ML sample, as the Sn coverage is too high and the number of O atoms is relatively limited, the Sn can only be oxidized to a charge of +1.4.

B. Thermal Stability of the SnO_x/Cu_2O/Cu(111) Surfaces: STM and XPS studies

To investigate the thermal stability of the SnO_x/Cu_2O/Cu(111) samples, annealing experiments were conducted under UHV at temperatures from 360 to 550 K with the previously described 0.2 ML sample. A noticeable change in morphology by annealing was observed at 550 K. Single-atom like SnO_x nanoclusters maintained their shape up to 450K (Figure 3b), with line defects in the copper oxide substrate trapping SnO_x particles. These started to aggregate and form big islands near step edges at 550 K (Fig 3c). The lateral size of the thermally induced SnO_x islands was found to vary, ranging from 10 to 50 nm. The average measured height was around 2.5 Å. In addition to the shape changes in the SnO_x component, variations in the structure of the Cu_2O film were clearly seen. The terrace (marked by the green trace) above the triangular SnO_x islands in Fig 3c displays a disappearance of the Cu_2O ordered structure, and the number of SnO_x

nanoclusters is scarce compared to that of the untreated 0.2 ML sample which showed the SnO_x clusters dominantly locate at the reduced area (See Fig 1c as comparison).

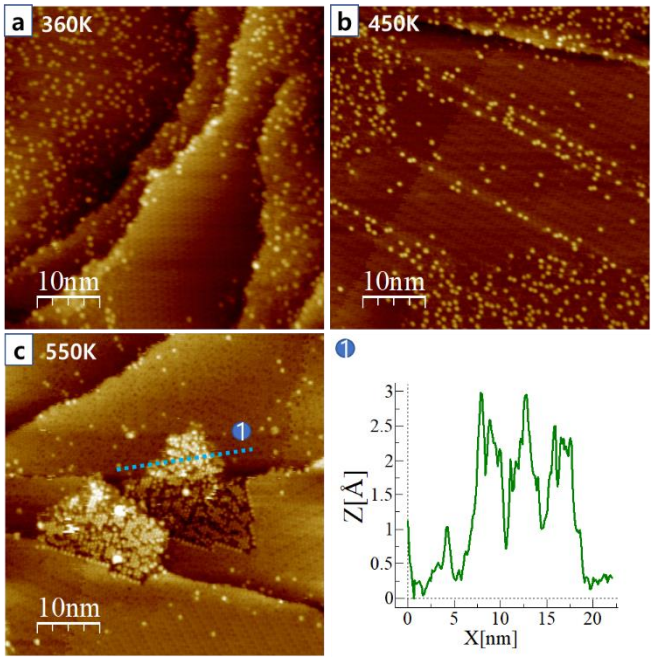

Fig. 3 Structural changes in the morphology of a 0.2 ML SnOx/Cu_2O/Cu(111) sample induced by annealing to high temperatures. (a) 360 K, 50 x 50 nm^2 (b) 450 K, 50 x 50 nm^2 (c) 550 K, 50 x 50 nm^2 (d) The line profile across the island in (c). Scanning conditions: (a) 0.1n A, -1.3 V (b) 0.1 nA, -1.2 V (c) 0.1 nA, -1.8 V.

Besides the STM study of morphological changes upon annealing, XPS was used to monitor the evolution in the chemical state of each component when heating from 300 to 500 K under UHV. For the plain Cu_2O/Cu(111) substrate, the O 1s XPS spectra are shown in Fig 4(a). At 450K, we observed the first oxygen loss due to the thermal decomposition of the Cu_2O overlayer, and it becomes more evident at 500 K. In comparison with the Cu_2O/Cu(111), the thermal stability of the 0.2 ML SnO_x/Cu_2O/Cu(111) sample was tested, as shown in Fig 4 (b) and (c). O_{Cu} is removed in a similar manner as observed for the plain Cu_2O/Cu(111) surface, whereas O_{Sn}, is stable and shows only minor losses at 500K. Such behavior was observed similarly when higher oxygen affinity metals than Cu were annealed to high temperatures.[54] For example, deposited ZrO_2 remains stable although the CuO_x/Cu(111) substrate loses its oxygen while annealing.[54] The annealing experiment shown above indicates that the SnO_2 nanostructures generated by self-oxidation are more thermally stable than the Cu_2O overlayer, and the interaction between Sn and O is stronger than that between Cu and O. Thus, it is not surprising that the Sn deposited onto the Cu_2O overlayer grabs O atoms to form SnO_2.

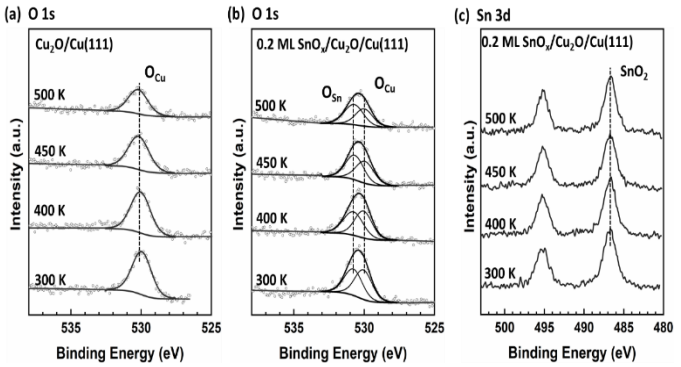

Fig. 4 (a) and (b) O 1s XPS region for the plain Cu_2O/Cu(111) substrate and a SnO_x/Cu_2O/Cu(111) surface (θ_{SnO2} ~ 0.2 ML) when annealing under UHV at different temperatures. (c) Corresponding Sn 3d XPS region for the SnO_x/Cu_2O/Cu(111) surface (θ_{SnO2} ~ 0.2 ML).

C. Theoretical Structure and Stability of SnO_2/Cu_2O/Cu(111): DFT Studies

To look into the SnO_x-CuO_x interactions, the SnO_2/Cu_2O/Cu(111) system was modeled using a three layer slab of a 4×4 Cu(111) surface with one monolayer of Cu_mO (m ≈ 1.13) and Sn_xO_{2x} (x =1,2,3 or 4) clusters deposited on top (Fig 5) to depict the small SnO_2 particles observed by STM (Fig 1). The experimental results indicate that the relative stability of the tin oxide clusters could change as a function of temperature and O_2 pressure. Thus, an ab initio thermodynamics analysis was performed to map the thermodynamically stable Sn_xO_{2x} clusters formed on a Cu_2O/Cu(111) model surface on exposure to O_2 gas and Sn vapor.

As shown in Fig 6, the phase diagram of Sn_xO_{2x}/Cu_2O/Cu(111) were plotted around the relevant experimental temperature and pressure range, in which Sn vapor pressure was set as the same pressure of O_2 gas. Upon the increasing of temperature and/or the decreasing of pressure, large clusters are thermodynamically likely to break into small clusters (Sn_4O_8, Sn_3O_6, Sn_2O_4) on Cu_2O/Cu(111) substrate (Fig. 6). This cannot be directly compared with the STM results by annealing under UHV conditions, as the diffusion and possible aggregation of Sn_xO_{2x} clusters over Cu_2O/Cu(111) at the elevated temperatures is not considered in the thermodynamic phase diagram. However, the consideration of binding energies of Sn_xO_{2x} clusters can help to bridge the gap. The binding energy of Sn_xO_{2x} varies from -53.27 kcal/mol of Sn_1O_2 to -55.34 kcal/mol of Sn_2O_4, -99.62 kcal/mol of Sn_3O_6 and -91.09 kcal/mol of Sn_4O_8. Given that, the small Sn_xO_{2x} clusters are likely more mobile and therefore aggregated by increasing system temperature than the large clusters. Thus, although with the increasing temperature the small Sn_xO_{2x} clusters are thermodynamically preferred to form

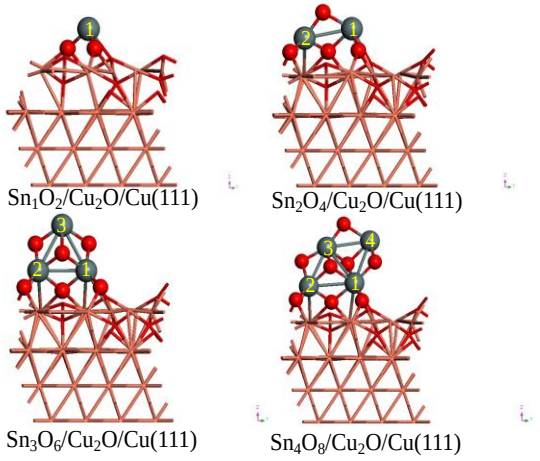

Fig. 5 DFT-optimized Sn_xO_{2x}/Cu_2O/Cu(111) systems; Cu: brown; Sn: dark green; O: red.

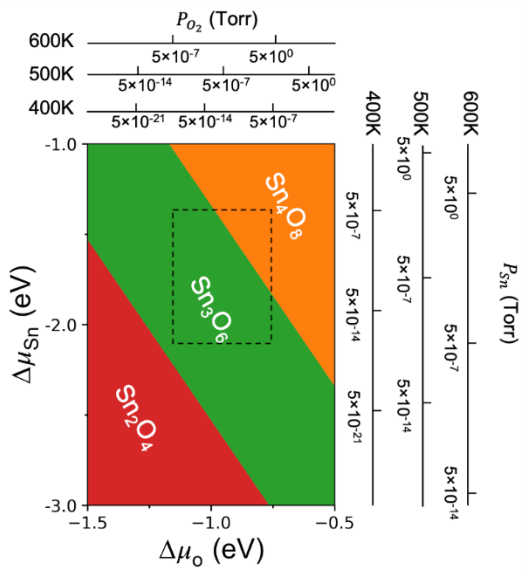

Fig. 6 Calculated relative stability of the Sn_1O_2, Sn_2O_4, Sn_3O_6 and Sn_4O_8 clusters on top of Cu_2O/Cu(111) based on ab initio thermodynamics as a function of the chemical potential potential of Sn and O, the pressures shown in the plots were set based on relevant experimental conditions and the dashed rectangular represented the most stable phases around a pressure of 5×10^{-7} Torr within the temperature range from 400K to 600K.

on Cu_2O/Cu(111), kinetically the increased mobility likely enhances the aggregation of growth of clusters as observed by STM. On the other hand, the strengthened Sn_xO_{2x}-Cu_2O/Cu(111) interaction for large cluster may impose kinetic barriers to hinder the thermodynamically favored decomposition to small clusters according to the phase diagram. There was no Sn_1O_2/Cu_2O/Cu(111) structure observed in the phase diagram due to its lower stability than the others. The dashed rectangular area labeled the most possible stable structures under our relevant experimental pressure (~5×10^{-7} Torr) and temperature (400K→600K), where Sn_3O_6/Cu_2O/Cu(111) was likely to be dominant and Sn_4O_8/Cu_2O/Cu(111) also coexisted. The supported Sn_3O_6 and Sn_4O_8 clusters adopted the size of 5.54 Å and 7.12 Å in diameter, respectively (Fig 5), which are both within the range observed using STM shown in Fig 1.

In addition, the DFT results also revealed that each Sn_xO_{2x} cluster were anchored on Cu_2O/Cu(111) via O at the Cu cation site and Sn at the O site (Fig 5). That is, the oxygen from both the surface and Sn_xO_{2x} are involved in the Sn_xO_{2x}-Cu_2O/Cu(111) interaction. Furthermore, according to the Bader charge analysis the Sn of supported Sn_1O_2 cluster was in the oxidation state of 2+ due to the transfer of electron density from Cu(111) to the SnO_2 cluster (Fig S3). With the increasing of cluster size, the Sn^{4+} emerged and the Sn^{4+}/Sn^{2+} was increased from 0 to 3. The stable Sn_3O_6 and Sn_4O_8 clusters identified based on the phase diagram (Fig 6) both corresponded to the dominance of Sn^{4+}, in consistence with the XPS observation (Fig 2), showing that the small Sn_xO_{2x} clusters formed at low coverage was dominated by Sn^{4+}. Given that, both Sn_3O_6/Cu_2O/Cu(111) and Sn_4O_8/Cu_2O/Cu(111) were used to study the catalytic activity toward CH_4 activation.

D. Methane Activation: AP-XPS studies

After knowing the thermal stability of the SnO_2/Cu_2O/Cu(111) surfaces, we further studied their activity for methane activation. It is well documented that CH_4 is a nonpolar molecule with highly stable C–H bonds, so its activation at low temperatures remains challenging [13,20]. As expected, we did not see any significant reduction for the Cu_2O/Cu(111) substrate at 300 K under 50 mTorr of CH_4 (see O 1s spectrum in Fig 7a). [19,20] When the surface is decorated by 0.2 ML SnO_2, we found that upon exposing to CH_4, the amount of O_{Sn} stays almost identical, implying that Sn was maintained in SnO_2 state. This conclusion is also confirmed by the Sn 3d spectra in Fig 7(b). In contrast, O_{Cu} decreases significantly, implying the reduction of Cu_2O. Comparing with the results from the control experiment, where Cu_2O/Cu(111) surface was not reduced by CH_4, we propose that the addition of SnO_2 can modify the surface, making it suitable for methane dissociating effectively at a temperature as low as 300 K. Once CH_4 is dissociated to CH_3* and H* atoms, H* will migrate to Cu_2O and remove O_{Cu}. The reaction can be described as shown below:

$$CH_4 \rightarrow {}^*CH_3 + {}^*H$$
$$2\,{}^*H + Cu_2O \rightarrow H_2O + 2Cu^0$$

This hypothesis is further confirmed by C 1s data, as shown in Fig 7(c). Exposing a Cu_2O/Cu(111) surface to 50 mTorr of CH_4 at 300 K resulted in two peaks at ~287.0 eV and 285.1 eV in the C 1s region, which we attribute to the CH_4 in gas phase and

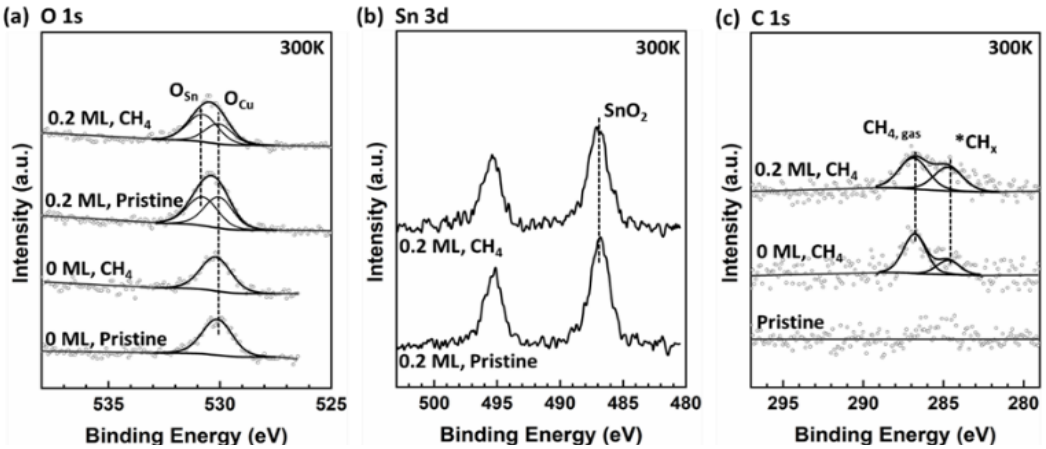

Fig. 7 (a) O 1s, (b) Sn 3d and (c) C 1s regions of AP-XPS spectra for the SnO_2/Cu_2O/Cu(111) surface (θ_{SnO2} ~ 0 or 0.2 ML) under different conditions at 300 K.

a minor amount of adsorbed *CH_x species [20,55], respectively. With the addition of SnO_2, the $^*CH_x$ peak increases significantly, indicating a more efficient dissociation of CH_4. It is worth noting that the CH_4 dissociation starts from a temperature as low as 300 K, indicating a low reaction barrier on such $SnO_2/Cu_2O/Cu(111)$ surface. DFT calculations further demonstrate the promoting effect of SnO_2 on methane activation with an activation energy as low as 18.45 kcal/mol (details shown below), in sharp contrast with the CH_4 activation energy of 36.90 kcal/mol on a bare and perfect $Cu_2O/Cu(111)$ surface[19]. Defects present in the $Cu_2O/Cu(111)$ substrate, see Fig 1a, are probably responsible for the small amount of dissociated methane seen in Fig 7c for the $CH_4/Cu_2O/Cu(111)$ system.

We also tested the CH_4 activation ability of the $SnO_x/Cu_2O/Cu(111)$ surface at temperatures ranging from 300 to 500 K. Fig 8(a) and (b) shows the corresponding O 1s and Sn 3d core-level spectra under 50 mTorr of CH_4, respectively. O_{Cu} is completely reduced at 400 K, at which temperature the O_{Sn} also starts to decrease. At 500 K, SnO_x is also reduced completely to the metallic state. It is crucial to note that at 400 and 450 K, the binding energy of Sn 3d is lowered by 0.2 eV. This fact implies that Sn may be in a +2 state, which is verified by the atomic O/Sn ratio (~ 1). Therefore, the Sn is in a hybrid state for the catalyst at 400 and 450 K, consisting of both SnO and Sn^0. In the C 1s region, the $^*CH_x$ peak increases drastically at 400 K and then reaches equilibrium at 450 K. The reduction of SnO_x and accumulation of $^*CH_x$ strongly suggests that CH_4 is activated on the surface at temperatures from 300 to 500 K.

Samples with 0.1 and 0.6 ML of SnO_x were also examined, and the results are shown in Fig S4 and S5, respectively. Briefly, they showed a similar trend as described for the 0.2 ML sample. The C 1s AP-XPS spectra acquired while exposing $Cu_2O/Cu(111)$ and several $SnO_x/Cu_2O/Cu(111)$ surfaces to 50 mTorr of CH_4 at 400 K were used to determine the effect of SnOx coverage on the amount of adsorbed $^*CH_x$ formed. After normalization to the intensity of the peak for gaseous CH_4, the most active $SnO_x/Cu_2O/Cu(111)$ systems were those with tin oxide coverages of 0.1 and 0.2 ML, as shown in Fig 9.

In addition, the SnO_x. coverage was found to influence the degree of reduction of the tin oxide and methane activation. With higher coverage, the SnO_x is more difficult to be reduced. For example, at 400 K under methane, ~23% of SnO_x was reduced to metallic on the 0.1 ML sample, while it was ~12% for 0.2 ML and 0 for 0.6 ML. These results can be related to the Sn-O-Cu interfacial sites. For 0.1 and 0.2 ML samples, Cu_2O could provide sufficient oxygen atoms to oxidize the deposited Sn, generating a SnO_2 phase and rich Sn-O-Cu interfacial sites. These interfacial sites are able to dissociate methane and are easier to be reduced, resulting in a higher $^*CH_x/CH_4$ ratio and better reducibility. However, in the case of the 0.6 ML sample, the surface O atoms of $Cu_2O/Cu(111)$ cannot fully oxidize such a high coverage of Sn. The Sn is only oxidized to a +1.4 state and this leads to a lack of interfacial Sn-O-Cu sites, which is responsible for the poor CH_4 activation and the reduced activity of the 0.6 ML sample.

As a short summary, we applied AP-XPS to understand the fundamental nature of the active sites responsible for C-H bond breaking on three $SnO_x/Cu_2O/Cu(111)$ systems. It is proposed that Sn has a strong interaction with Cu_2O, thus leading to self-oxidation and creating a Sn-O-Cu interface. The sites in this interface are chemically active and cleave the C-H bonds in methane at temperatures between 300-500 K. Under a real catalytic reaction, like methane dry reforming ($CH_4+CO_2 \rightarrow 2CO + 2H_2$) or methane partial oxidation ($CH_4 + 0.5O_2 \rightarrow CH_3OH$), the oxidant in the reaction feed should maintain tin as an oxide, preventing any deactivation due to the generation of fully reduced Sn.

E. Methane Activation on $SnO_2/Cu_2O/Cu(111)$: DFT studies

In a previous theoretical study, a CH_4 activation energy of 36.90 kcal/mol was calculated on a bare and perfect $Cu_2O/Cu(111)$ surface[19]. In this work, DFT calculations were also performed to understanding the CH_4 activation over two

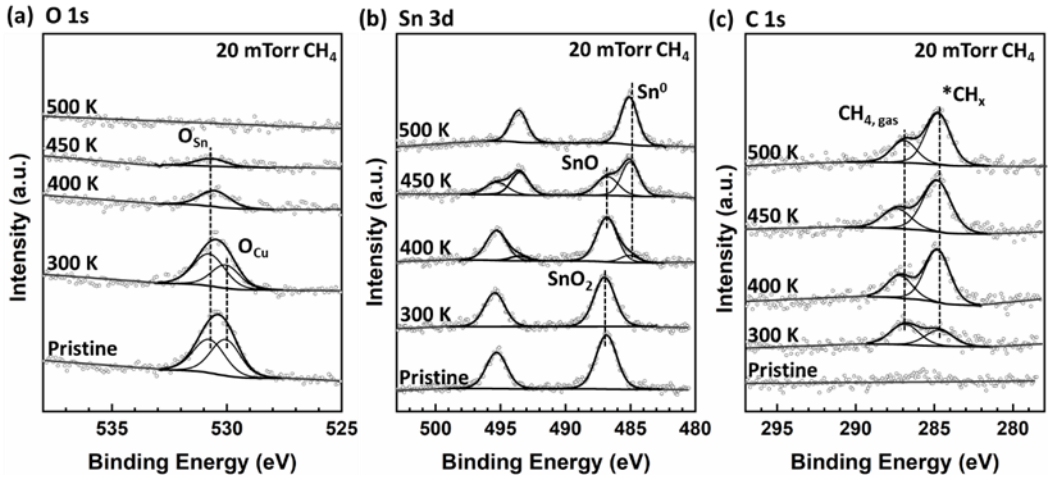

Fig. 8 (a) O 1s, (b) Sn 3d, and (c) C 1s regions in AP-XPS spectra for the $SnO_2/Cu_2O/Cu(111)$ surface (θ_{SnO2} ~ 0.2 ML) when exposed to 50 mTorr of CH_4 at different temperatures.

identified stable systems, $Sn_3O_6/Cu_2O/Cu(111)$ and

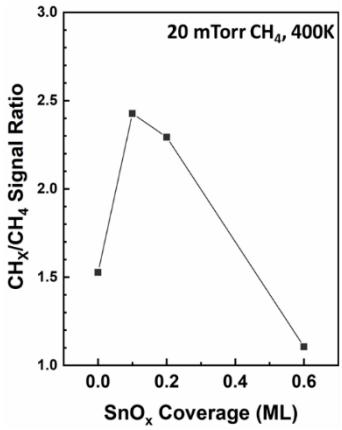

Fig. 9 Comparison of the concentration of adsorbed $^{*}CH_x$ on $Cu_2O/Cu(111)$ and several $SnO_x/Cu_2O/Cu(111)$ surfaces. The corresponding C 1s intensities were taken from Figs 8, S3 and S4.

$Sn_4O_8/Cu_2O/Cu(111)$ (Figs 5 and 6). The results showed that CH_4 preferred to adsorb at the bridging O site located between Sn^{4+} and Sn^{2+} of $Sn_4O_8/Cu_2O/Cu(111)$ with an adsorption energy (E_{ads}) of -0.69 kcal/mol (Fig 10). The corresponding dissociation of CH_4 was highly exothermic (ΔE = -36.21 kcal/mol) with an activation barrier (E_a) of 18.45 kcal/mol. Similarly for $Sn_3O_6/Cu_2O/Cu(111)$, such Sn^{4+}-Sn^{2+} bridged O site was also favored by CH_4 with the same binding energy adopted. The difference compared to $Sn_4O_8/Cu_2O/Cu(111)$ was that the corresponding dissociation was less exothermic (ΔE = -32.29 kcal/mol) with a slightly higher activation barrier (E_a = 22.14 kcal/mol) (Fig 10). The slightly higher activity of supported Sn_4O_8 than Sn_3O_6 was associated with the higher-lying density of bridging O 2p states toward the Fermi level (Fig 11). According to our previous studies[20,56], such oxygen species were more active for stabilization of transition state and intermediate during CH_4 dissociation, which was also observed in this case (Fig 10). In addition, the more significant down-shift of O 2p on interaction with $*CH_3$ observed for $Sn_4O_8/Cu_2O/Cu(111)$ than that for $Sn_3O_6/Cu_2O/Cu(111)$ also confirmed the stronger $*CH_3$- $Sn_4O_8/Cu_2O/Cu(111)$ interaction (Fig 11). Nevertheless, the deposition of Sn_4O_8 and Sn_3O_6 clusters on $Cu_2O/Cu(111)$ enables the promotion to methane activation by lowering the activation energy by at least 14 kcal/mol,[19] which well described the XPS results (Fig 9).

According to our DFT calculations, the bridging O site was slightly more active on $Sn_4O_8/Cu_2O/Cu(111)$ than that on the smaller cluster, $Sn_3O_6/Cu_2O/Cu(111)$, though the local coordination, Sn^{4+}-Sn^{2+} bridge, was the same. Such activity difference is associated by the intrinsic structural properties of the supported Sn_xO_{2x} clusters. To demonstrate that, the formation energy (E_{Ov}) of the oxygen vacancy (O_v) was calculated by removing the active bridging oxygen involved in CH_4 dissociation (Fig S6). The results showed that the oxygen removal from $Sn_4O_8/Cu_2O/Cu(111)$ (E_{Ov} = 20.75 kcal/mol) was thermodynamically easier than that of $Sn_3O_6/Cu_2O/Cu(111)$ (E_{Ov} =31.82 kcal/mol). Upon O_v formation, there was not much structural change observed for $Sn_3O_5/Cu_2O/Cu(111)$; while in the case of $Sn_4O_7/Cu_2O/Cu(111)$ the Sn^{2+} displayed higher mobility, which slightly shifted away from the cluster and drove the neighboring oxygen to migrate from the Sn hollow site toward the O_v site (Fig S5). In this way, the supported Sn_4O_7 cluster was stabilized more significantly than that of Sn_3O_5. Such mobility of Sn^{2+} seen for the supported Sn_4O_8 ensures the observed activity of the interacted bridging oxygen toward CH_4 dissociation, which can also explain well the relatively high reducibility of small SnO_2 clusters at low coverage observed by XPS (Fig S3). Here, we note that the difference in CH_4 dissociation activity between $Sn_4O_8/Cu_2O/Cu(111)$ and $Sn_3O_6/Cu_2O/Cu(111)$ is not significant (~4 kcal/mol in E_a, Fig 10) and easily can be erased at temperatures between 300 and 500 K. In this temperature range, both clusters of tin oxide should be very efficient for the activation of methane.

In recent years, many theoretical studies have addressed the activation of methane on solid surfaces. [13,57–60] Pure metal surfaces are not efficient for the activation of this light alkane,[13,61] exhibiting low binding energies and high activation barriers for C-H bond cleavage that do not compare well with those calculated on the $Sn_xO_{2x}/Cu_2O/Cu(111)$ systems (Fig 10). These systems have thermochemical parameters for methane activation that match those found for some oxide or metal/oxide systems which are able to activate well the molecule.[13,55,59,60,62] They are not as impressive as those

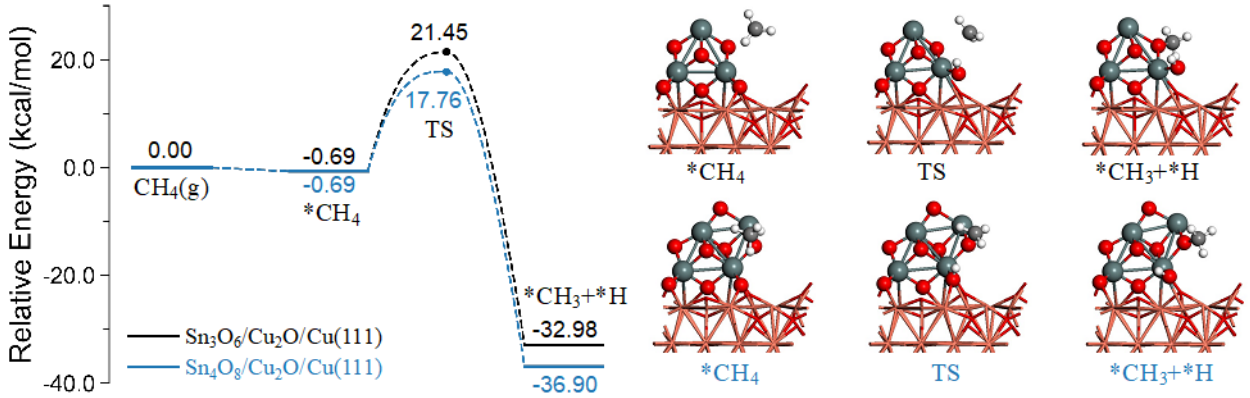

Fig 10. DFT-calculated potential energy diagram and intermediates and transition states (TS) structures for CH_4 activation on $SnO_2/Cu_2O/Cu(111)$ model catalysts with different size Sn_xO_y clusters; Cu: brown; Sn: dark green; O: red; C: gray; H: white.

calculated for dissociation of the molecule on $IrO_2(110)$,[57] where C-H bond cleavage occurs as a temperature as low as 150 K. Nevertheless, the room-temperature activation of methane seen on $Sn_xO_{2x}/Cu_2O/Cu(111)$ is remarkable and this oxide-oxide interface has the potential for being useful in the conversion of methane to high value chemicals.

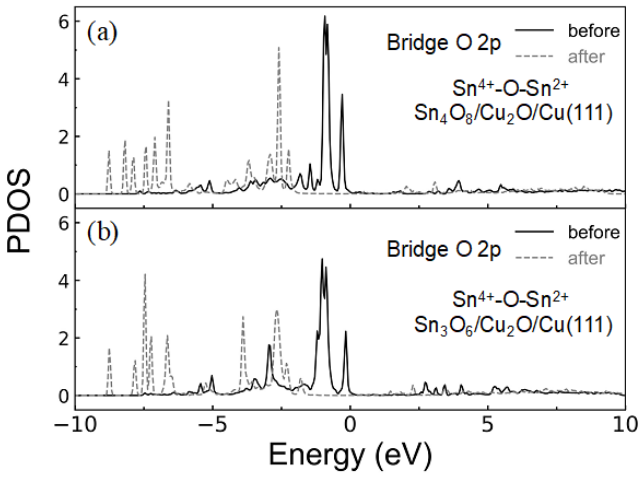

Fig. 11 Partial density of states (PDOS) of bridging O 2p located at the Sn^{4+}-Sn^{2+} bridge of $Sn_4O_8/Cu_2O/Cu(111)$ model (a) and $Sn_3O_6/Cu_2O/Cu(111)$ model (b) before and after CH_4 dissociation.

Conclusions

Varying the SnO_x coverage, a series of $SnO_x/Cu_2O/Cu(111)$ surfaces were prepared by vapor depositing tin on $Cu_2O/Cu(111)$ at 450 K in an oxygen ambient. The $SnO_x/CuOx/Cu(111)$ systems were characterized by STM and XPS. They exhibited well-dispersed nanoclusters having ~8 Å in size and ~1.3Å in height, and the chemical state of these clusters was determined to be Sn^{4+}. The SnO_x-Cu_2O interface is generated via strong Sn-O interaction on top of the Cu_2O overlayer. The results of AP-XPS showed that the $SnO_2/CuO_2/Cu(111)$ systems activate CH_4 at low and moderate temperatures (300 - 500K), leading to hydrocarbon formation on the oxide surfaces. Low coverages of SnO_x with a rich SnO_x-Cu_2O interface were found to be the most active for this reaction. An ab initio thermodynamics analysis-based phase diagram identified that the most likely SnO_x species observed by STM are Sn_3O_6 and Sn_4O_8 clusters, which are central for the CH_4 activation process. Furthermore, DFT calculations showed a drastic reduction in the activation barrier for C-H bond cleavage when going from $Cu_2O/Cu(111)$ to $SnO_x/Cu_2O/Cu(111)$. On the supported SnO_x clusters, the dissociation of methane was highly exothermic (ΔE ~ -35 kcal/mol) and the calculated barrier for activation (~ 20 kcal/mol) could be overcome at 300-500 K, target temperatures for the conversion of methane to high value chemicals.

Author Contributions

J. K., Y. T., M. M, and R. S carried out STM experiments; N. R., R. R, and I. O. performed XPS measurements; E. H. carried out theoretical computations. S.S., P.L. and J.R. supervised the experimental and theoretical work. J. K., R. N., E. H., P. L., and J. R. wrote the paper. All authors discussed the results, commented on the paper, and have given approval to the final version of the manuscript.

Conflicts of interest

There are no conflicts to declare.

Acknowledgements

The research was carried out at Brookhaven National Laboratory (BNL) and supported by the division of Chemical Science, Geoscience, and Bioscience, Office of Basic Energy Science of the US Department of Energy (DOE) under Contract No. DE-SC0012704. The DFT calculations were performed using computational resources at Center for Functional Nanomaterials (CFN), and the Scientific Data and Computing Center, a component of the Computational Science Initiative, at BNL under Contract No. DE-SC0012704, at the National Energy Research Scientific Computing Center (NERSC), a DOE Office of Science User Facility, supported by the Office of Science of the DOE under contract DE-AC02-05CH11231 and at Stony Brook University, which was founded by National Science Foundation grant (#1531492).

References

1 E. McFarland, *Science*, 2012, **338**, 341–342.
2 P. Tang, Q. Zhu, Z. Wu and D. Ma, *Energy Environ. Sci.*, 2014, **7**, 2580–2591.
3 Q. Liu, M. Luo, Z. Zhao and Q. Zhao, *Chem. Eng. J.*, 2020, **380**, 122423.
4 L. Luo, J. Luo, H. Li, F. Ren, Y. Zhang, A. Liu, W.-X. Li and J. Zeng, *Nat. Commun.*, 2021, **12**, 1218.
5 M. B. Park, E. D. Park and W.-S. Ahn, *Front. Chem.*, 2019, **1**, 514.
6 Y. Kwon, T. Y. Kim, G. Kwon, J. Yi and H. Lee, *J. Am. Chem. Soc*, 2017, **139**, 17694–17699.
7 L. Arnarson, P. S. Schmidt, M. Pandey, A. Bagger, K. S. Thygesen, I. E. L. Stephens and J. Rossmeisl, *Phys. Chem. Chem. Phys*, 1115, **20**, 11152.
8 M. Ravi, V. L. Sushkevich, A. J. Knorpp, M. A. Newton, D. Palagin, A. B. Pinar, M. Ranocchiari and J. A. van Bokhoven, *Nat. Catal.*, 2019, **2**, 485–494.
9 C. Rameshan, H. Li, K. Anic, M. Roiaz, V. Pramhaas, R. Rameshan, R. Blume, M. Hävecker, J. Knudsen, A. Knop-Gericke and G. Rupprechter, *J. Phys. Condens. Matter*, 2018, **30**, 264007.
10 L. Shi, G. Yang, K. Tao, Y. Yoneyama, Y. Tan and N. Tsubaki, 2021, **37**, 42.
11 Y. Matsumura and T. Nakamori, *Appl. Catal. A Gen.*, 2004, **258**, 107–114.

12 L. Sun, Y. Wang, N. Guan and L. Li, *Energy Technol.*, 2020, **8**, 1900826.
13 S. D. Senanayake, J. J. Rodriguez and J. F. Weaver, *Acc. Chem. Res.*, 2020, **53**, 1488–1497.
14 P. Schwach, X. Pan and X. Bao, *Chem. Rev.*, 2017, **117**, 8497–8520.
15 P. G. Lustemberg, R. M. Palomino, R. A. Gutiérrez, D. C. Grinter, M. Vorokhta, Z. Liu, P. J. Ramírez, V. Matolín, M. V. Ganduglia-Pirovano, S. D. Senanayake and J. A. Rodriguez, *J. Am. Chem. Soc.*, 2018, **140**, 7681–7687.
16 S. I. Chan and S. S. F. Yu, *Acc. Chem. Res.*, 2008, **41**, 969–979.
17 V. C. C. Wang, S. Maji, P. P. Y. Chen, H. K. Lee, S. S. F. Yu and S. I. Chan, *Chem. Rev.*, 2017, **117**, 8574–8621.
18 M. Ravi, M. Ranocchiari and J. A. van Bokhoven, *Angew. Chemie - Int. Ed.*, 2017, **56**, 16464–16483.
19 Z. Zuo, P. J. Ramírez, S. D. Senanayake, P. Liu and J. J. Rodriguez, *J. Am. Chem. Soc.*, 2016, **138**, 13810-13813
20 Z. Liu, E. Huang, I. Orozco, W. Liao, R. M. Palomino, N. Rui, T. Duchoň, S. Nemšák, D. C. Grinter, M. Mahapatra, P. Liu, J. A. Rodriguez and S. D. Senanayake, *Science*, 2020, **368**, 513–517.
21 G. Fedorenko, L. Oleksenko, N. Maksymovych, G. Skolyar and O. Ripko, *Nanoscale Res. Lett.*, 2017, **12**, 329.
22 M. Batzill, *Sensors*, 2006, **6**, 1345–1366.
23 U. Guharoy, E. Le Saché, Q. Cai, T. R. Reina and S. Gu, *J. CO2 Util.*, 2018, **27**, 1–10.
24 E. Nikolla, J. Schwank and S. Linic, *J. Catal.*, 2009, **263**, 220–227.
25 L. Zhang, Y. Hu, W. Xu, C. Huang, Y. Su, M. Tian, Y. Zhu, H. Gong and X. Wang, *Energy Fuels*, 2020, **34**, 6991-6998
26 C. Liu, H. Xian, Z. Jiang, L. Wang, J. Zhang, L. Zheng, Y. Tan and X. Li, *Appl. Catal. B Environ.*, 2015, **176-177**, 542–552.
27 H. Bluhm, M. Hävecker, A. Knop-Gericke, E. Kleimenov, R. Schlögl, D. Teschner, V. I. Bukhtiyarov, D. F. Ogletree and M. Salmeron, *J. Phys. Chem. B*, 2004, **108**, 14340–14347.
28 S. Sá, H. Silva, L. Brandão, J. M. Sousa and A. Mendes, *Appl. Catal. B Environ.*, 2010, **99**, 43–57.
29 M. Behrens, F. Studt, I. Kasatkin, S. Kühl, M. Hävecker, F. Abild-pedersen, S. Zander, F. Girgsdies, P. Kurr, B. Kniep, M. Tovar, R. W. Fischer, J. K. Nørskov and R. Schlögl, 2012, **759**, 893–898.
30 J. Graciani, K. Mudiyanselage, F. Xu, A. E. Baber, J. Evans, S. D. Senanayake, D. J. Stacchiola, P. Liu, J. Hrbek, J. Fernández Sanz and J. A. Rodriguez, *Science*, 2014, **345**, 546–550.
31 M. Mahapatra, J. Kang, P. J. Ramírez, R. Hamlyn, N. Rui, Z. Liu, I. Orozco, S. D. Senanayake and J. J. Rodriguez, *J. Phys. Chem. C*, 2018, **122**, 53.
32 M. Mahapatra, R. A. Gutiérrez, J. Kang, N. Rui, R. Hamlyn, Z. Liu, I. Orozco, P. J. Ramírez, S. D. Senanayake and J. A. Rodriguez, *Surf. Sci.*, 2019, **681**, 116–121.
33 Hohenbergt P and W. Konnt, *Phys. Rev.*, 1964, **136**, B864-871.
34 W. Kohn and L. J. Sham, *Phys. Rev.*, 1965, **140**, A1133–A1138.
35 G. Kresse and J. Furthmüller, *Phys. Rev. B - Condens. Matter Mater. Phys.*, 1996, **54**, 11169–11186.
36 P. E. Blöchl, *Phys. Rev. B*, 1994, **50**, 17953–17979.
37 G. Kresse and D. Joubert, *Phys. Rev. B*, 1999, **59**, 1758–1775.
38 J. P. Perdew, K. Burke and M. Ernzerhof, *Phys. Rev. Lett.*, 1996, **77**, 3865–3868.
39 H. J. Monkhorst and J. D. Pack, *Phys. Rev. B*, 1976, **13**, 5188–5192.
40 G. Henkelman and H. Jónsson, *J. Chem. Phys.*, 2000, **113**, 9978–9985.
41 S. Dudarev and G. Botton, *Phys. Rev. B - Condens. Matter Mater. Phys.*, 1998, **57**, 1505–1509.
42 A. E. Baber, X. Yang, H. Y. Kim, K. Mudiyanselage, M. Soldemo, J. Weissenrieder, S. D. Senanayake, A. Al-Mahboob, J. T. Sadowski, J. Evans, J. A. Rodriguez, P. Liu, F. M. Hoffmann, J. G. Chen and D. J. Stacchiola, *Angew. Chemie - Int. Ed.*, 2014, **53**, 5336–5340.
43 K. Reuter and M. Scheffler, *Phys. Rev. B*, 2001, **65**, 035406.
44 K. Reuter and M. Scheffler, *Phys. Rev. B - Condens. Matter Mater. Phys.*, 2003, **68**, 045407.
45 NIST Computational Chemistry Comparison and Benchmark Database, https://cccbdb.nist.gov/, (accessed 25 May 2021).
46 F. Yang, S. Kundu, A. B. Vidal, J. Graciani, P. J. Ramírez, S. D. Senanayake, D. Stacchiola, J. Evans, P. Liu, J. F. Sanz and J. A. Rodriguez, *Angew. Chemie - Int. Ed.*, 2011, **50**, 10198–10202.
47 F. Yang, J. us Graciani, J. Evans, P. Liu, J. Hrbek, J. Fdez Sanz and J. A. Rodriguez, *J. Am. Chem. Soc*, 2011, **133**, 3444–3451.
48 T. Matsumoto, R. A. Bennett, P. Stone, T. Yamada, K. Domen and M. Bowker, *Surf. Sci.*, 2001, **471**, 225–245.
49 I. Orozco, E. Huang, M. Mahapatra, R. Shi, J. Kang, S. Nemšák, S. D. Senanayake, P. Liu and J. A. Rodriguez, *J. Phys. Chem. C*, 2021, **125**, 558–571.
50 F. Jensen, F. Besenbacher, E. Lægsgaard and I. Stensgaard, *Surf. Sci. Lett.*, 1991, **259**, L774–L780.
51 J. A. Taylor, G. M. Lancaster and J. W. Rabalais, *J. Electron Spectros. Relat. Phenomena*, 1978, **13**, 435–444.
52 H. Willemen, D. F. Van De Vondel and G. P. Van Der Kelen, *Inorganica Chim. Acta*, 1979, **34**, 175–180.
53 J. H. Scofield, *J. Electron Spectros. Relat. Phenomena*, 1976, **8**, 129–137.
54 R. Shi, M. Mahapatra, J. Kang, I. Orozco, S. D. Senanayake and J. A. Rodriguez, *J. Phys. Chem. C*, 2020, **124**, 10502–10508.
55 P. G. Lustemberg, R. M. Palomino, R. Ramón, A. Gutiérrez, D. C. Grinter, M. Vorokhta, Z. Liu, P. J. Ramírez, V. Matolín, M. V. Ganduglia-Pirovano, S. D. Senanayake and J. A. Rodriguez, *J. Am. Chem. Soc.*, 2018, **140**, 7681-7687
56 I. Orozco, E. Huang, M. Mahapatra, J. Kang, R. Shi, S. Nemšák, X. Tong, S. D. Senanayake, P. Liu and J. A. Rodríguez, *J. Phys. Chem. C*, 2021, **125**, 6673-6683.
57 Z. Liang, T. Li, M. Kim, A. Asthagiri and J. F. Weaver, 2017.
58 Z. Liu, D. C. Grinter, P. G. Lustemberg, T. D. Nguyen-Phan, Y. Zhou, S. Luo, I. Waluyo, E. J. Crumlin, D. J. Stacchiola, J.

Zhou, J. Carrasco, H. F. Busnengo, M. V. Ganduglia-Pirovano, S. D. Senanayake and J. A. Rodriguez, *Angew. Chemie - Int. Ed.*, 2016, **55**, 7455–7459.

59 V. Fung, F. Tao and D. Jiang, *Phys. Chem. Chem. Phys*, 2018, **20**, 22909.

60 M. Figueras, R. A. Gutiérrez, H. Prats, F. Viñes, P. J. Ramírez, F. Illas and J. A. Rodriguez, *Phys. Chem. Chem. Phys.*, 2020, **22**, 7110–7118.

61 J. F. Weaver, A. F. Carlsson and R. J. Madix, *Surf. Sci. Rep.*, 2003, **50**, 107–199.

62 P. G. Lustemberg, F. Zhang, R. A. Gutiérrez, P. J. Ramírez, S. D. Senanayake, J. A. Rodriguez and M. V. Ganduglia-Pirovano, *J. Phys. Chem. Lett.*, 2020, **11**, 9131–9137.